Journal of Aeronautics and Space Technologies

16(1) (2023) 64-79

Journal Homepage: jast.hho.msu.edu.tr

RESEARCH ARTICLE

Leading-Edge Vortex Characteristics of Surging-Translating Flexible Wings

Doğrusal Öteleme Hareketi Yapan Kanatlarda Hücum Kenarı Girdabı Karakteristiği

Mahdi Yazdanpanah[1], Mustafa Perçin[2*]

[1] *Middle East Technical University, Department of Aerospace Engineering, 06800 Ankara, Türkiye,*
[2] *Middle East Technical University, Center for Wind Energy Research (RÜZGEM), 06800 Ankara, Türkiye*

Received: *January 10, 2022* ***Revised:*** *September 21, 2022* ***Accepted:*** *December 13, 2022*

Abstract

This study experimentally investigates the flow fields around rigid and chordwise-flexible wings, performing a rectilinear translational motion starting from rest. A rigid wing and two flexible wings with an intermediate degree of flexibility and a high degree of flexibility are considered in this study. Phase-locked planar particle image velocimetry measurements are performed at the 75% span position of the wings at the Reynolds number of 7360. The results reveal the presence of a coherent LEV and a series of vortices shedding from the trailing edge of the wing in the acceleration phase. At the late stages of the constant-speed phase, the LEV moves away from the wing surface and bursts into smaller flow structures in the case of the rigid wing and the wing with an intermediate degree of flexibility. In the case of the wing with a high degree of flexibility, a smaller geometric angle of attack is attained due to a larger chordwise deformation of the wing, resulting in a coherent LEV positioned close to the wing surface throughout the motion. A stable LEV and the associated low-pressure region and the increased size of the horizontal surface area may elevate the resultant lift force.

Keywords: Leading-Edge Vortex, Particle Image Velocimetry, Chordwise-Flexible Wings

Özet

Bu çalışma, durağanlıktan başlayarak doğrusal öteleme hareketi gerçekleştiren rijit ve veter yönünde esnek kanatlar etrafındaki akış alanlarını deneysel olarak araştırmaktadır. Bu çalışmada bir rijit kanat ve orta derecede esnekliğe ve yüksek derecede esnekliğe sahip iki esnek kanat ele alınmıştır. Faz kilitli düzlemsel parçacık görüntülemeli hız ölçümleri, 7360 Reynolds sayısında kanatların %75 açıklık konumunda gerçekleştirilmiştir. Sonuçlar, ivmelenme fazında belirgin bir hücum kenarı girdabının (HKG) ve firar kenarından seri halde kopan girdapların varlığını göstermektedir. Sabit hız fazının geç aşamalarında, HKG kanat yüzeyinden uzaklaşmakta ve rijit kanat ile orta derecede esnek kanat durumunda daha küçük akış yapılarına dönüşmektedir. Yüksek derecede esnekliğe sahip kanat durumunda ise, kanadın veter yönündeki daha büyük deformasyonu nedeniyle daha küçük bir geometrik hücum açısı elde edilmekte; bu da hareket boyunca kanat yüzeyine yakın konumlandırılmış tutarlı bir HKG ile sonuçlanmaktadır. Sabit bir HKG ve ilgili düşük basınç bölgesi ile yatay yüzey alanının artan boyutu, ortaya çıkan taşıma kuvvetini yükseltebilir.

Anahtar Kelimeler: Hücum Kenarı Girdabı, Parçacık Görüntülemeli Hız Ölçme, Veter Yönünde Esnek Kanatlar

*Corresponding Author
E-mail: mpercin@metu.edu.tr

1. INTRODUCTION

Nature has been a source of inspiration in the technical evolution of airborne vehicles for a long time. Parallel to the progress in the discipline of micro air vehicles (MAVs), the number of studies focusing on the biological flapping-wing flight has increased because aerodynamic mechanisms inherent to fixed and rotary wing flight become inefficient at the typical low Reynolds number regime ($Re < 10^5$) of MAV operations [1]. In contrast to well-known force production mechanisms of fixed and rotary wing aerodynamics, the flapping-wing flight utilizes unconventional aerodynamic mechanisms. The formation of a stable leading-edge vortex (LEV) and the associated low-pressure region has proven to be one of the most dominant force production mechanisms in flapping-wing aerodynamics [2]. Muijres et al. [3] showed that LEVs could produce up to 50% of the total lift on the wings.

Biological flyers move their wings to hover or perform a maneuver through a combination of three main motions, known as plunging, sweeping, and pitching. Accordingly, the flow around flapping wings is highly three-dimensional and unsteady. In the literature, each of these individual motions has been investigated to comprehensively understand the fundamental mechanisms of flapping-wing flight. The sweeping motion is emulated by either a rectilinear translational motion or a revolving motion. The flow separates from the leading edge and reattaches to the surface of the wing in a revolving motion, leading to the formation of an LEV. The flow then leaves the trailing edge tangentially so that the Kutta condition is still preserved [2]. The LEV does not shed into the wake but moves with the wing yielding a sustained lift generation. The stability of the LEV in a revolving motion is attributed to the rotational inertial mechanisms [4] in combination with the spanwise flow [5]. On the other hand, in a translational motion, an LEV still forms and grows in strength, but it does not remain attached for a long time [2]. The comparison of the two motion kinematics has been the subject of a number of studies. Ol and Babinsky [6] reviewed these studies and observed that a stable LEV exists in wings undergoing a revolving motion. The translating wings had a drop in the lift values after a specific length of travel. In contrast, the lift values remained around a constant value in revolving wings, which justifies the persistence of stable LEV in revolving wings [6].

In mechanical simulations of natural flyers, wing flexibility is often disregarded, which is an important factor in the formation of flow fields around wings and lift generation. Considering the wing flexibility, the investigation of flapping wings can be quite complicated due to the wing deformations during different maneuvers. Different studies on this topic have shown the possible advantages of the use of flexible wings on the aerodynamic performance of flapping wings [7]. Zhao et al. [8] showed that wing flexibility does not alter the overall flow topology; however, the size of the LEV is smaller for flexible wings. Relatively small aerodynamic forces are produced as the size of the LEV becomes smaller. Beals and Jones [9] investigated the lift production of a rigid wing and a wing with chordwise flexibility comprised of two rigid panels linked at the middle of the chord performing a rotational

motion. It was observed that despite the relatively low lift production, the flow-induced structural deformation of the flexible wing alleviates the lift losses in the second revolution when the wing passes through its own wake. It can be concluded that chordwise flexibility is a profitable feature for the wings operating in unsteady flows. Mountcastle and Daniel [10] and Eldredge et al. [11] showed that wing flexibility is considered to be a significant feature in enhancing the aerodynamic performance in flapping-wing flight. In their experiments, van de Meerendonk et al. [12] used the same wings that are used in the present study but in a revolving motion. They showed that the most flexible wing has the highest lift-to-drag ratio, which displays a beneficial aspect of wing flexibility in terms of aerodynamic performance.

In this respect, the main objective of this study is to investigate the effects of wing flexibility on the leading-edge vortex and the flow topology in surging-translating wings. For this purpose, three wing models with different flexural stiffness values (rigid, intermediate degree of flexibility and high degree of flexibility) are tested in this study. Phase-locked planar particle image velocimetry measurements are performed at the 75% span position to obtain the planar flow fields.

2. METHODOLOGY

2.1. Experimental Setup and Wing Models

The experiments are conducted in an octagonal water tank located at the Aerospace Engineering Department of Middle East Technical University. A robotic arm with three degrees of freedom (translational motion in the x and y directions and rotational motion about the z-axis) is used to drive the wing models in surging-translating motion. The PIV cameras are located on a plate that translates with the robotic arm mechanism; thus, the field of view and the wing leading edge position in the camera images at all stages of the motion are identical.

The wing models are essentially rectangular flat plates with a leading edge that is made of a carbon-fiber rod to provide rigidity in the spanwise direction. The chord (c) and span (b) lengths of the models are 92 mm and 184 mm, respectively, yielding an aspect ratio of 2. The leading edge carbon rod is extended at the wing root, and it is fixed into an adapter that connects the wing model to the robotic arm (see Figure 1). A carbon fiber rod is also integrated into the rigid wing to have the same leading-edge geometry for all the wing models.

The flexural stiffness (EI) is utilized as a measure of wing flexibility. By definition, it consists of two parameters: Young's modulus (E) of the wing material and the area moment of inertia ($I = Rh^3/12$), where,h is the thickness of the wing, and R is the span of the wing. The non-dimensional bending stiffness parameter (Π_1) is used to scale the elastic bending forces to fluid dynamic forces exerting on the model as follows [7]:

$$\Pi_1 = \frac{E h^3}{12(1-\nu^2)\rho {V_t}^2 c^3} \tag{1}$$

where ν is the Poisson ratio, ρ is the fluid density, and V_t is the terminal velocity. This study considers three different models with different flexural stiffness values, as reported in Table 1. The acrylic glass wing is practically regarded as rigid. By altering the thickness of the material, the flexural stiffness of the flexible wings can be changed.

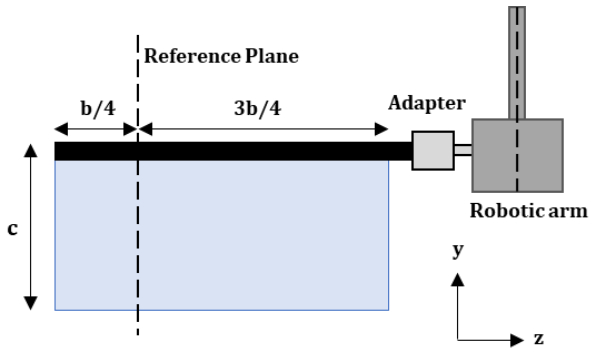

Figure 1. The schematic view of the wing model.

Table 1. Properties of the wing models.

Wing model	Material	Young's modulus (E) [N/m²] × 10^6	Thickness h [μm]	Flexural stiffness (EI) [Nm²] × 10^{-4}	Π_1
Rigid	Acrylic glass	≈ 3300	1000	506	65.5
Intermediate degree of flexibility	Polyethylene terephthalate	≈ 4350	175	3.57	0.46
High degree of flexibility	Polyethylene terephthalate	≈ 4500	125	1.34	0.17

For acrylic glass and polyethylene terephthalate, a Poisson ratio of 0.4 is utilized in the definition of Π_1. The water density (ρ) is assumed as 1000 (kg/m³).

It was shown by Percin et al. [13] that the aeroelastic characteristics of flexible wings in-air and in-water working mediums are notably different. A full aeroelastic scaling requires similarity between the Reynolds number (Re), the bending stiffness (Π_1), and the inertia parameter (Π_2), which represents the ratio of inertial forces to fluid-dynamic forces [8]:

$$\Pi_2 = \frac{\rho_{surface}}{\rho_{fluid}} \frac{h}{c} \tag{2}$$

The similarity in terms of the Re and the bending stiffness parameter (Π_1) can be achieved by tuning the wing velocity and the dimensions of the wing when switching the medium from air to water. The inertial parameter (Π_2), on the other hand, is decreased by a factor of 800

due to the increase in the fluid density, which means that the wing behaves much lighter in water compared to air. As an example, for the wing with a high degree of flexibility considered in this study, $\Pi_2 \approx 0.002$ for the current in-water experiment and $\Pi_2 \approx 1.6$ for a scaled wing in air. This difference indicates that the inertial effects are influential on the wing deformations in air, and they are negligible in water experiments. This is an inevitable limitation of scaling of wing flexibility between in-air and in-water conditions.

2.2. Surging-Translating Motion Kinematics

The wing models are driven in a rectilinear motion at a fixed initial geometric angle of 45°. The motion kinematics is comprised of an acceleration phase from rest to the terminal velocity of $V_t = 0.08\ m/s$ (corresponding to a Reynolds number of 7360 based on the wing chord length) over one chord length of travel ($\delta^* = \delta/c = 1$, where δ is the distance traveled by the wing) or in other words, over a convective time of $t^* = 2$ ($t^* = t \times V_t/c$, where t is the time). Subsequently, the wing continues to translate at the constant terminal velocity for three more chord lengths (i.e., $1 < \delta^* < 4$), as shown Figure 2.

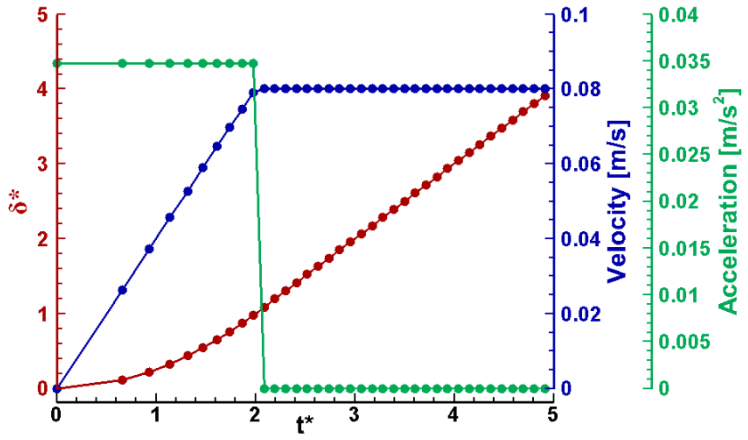

Figure 2. Surging-translating motion kinematics.

2.3. Experimental Setup for PIV Measurements

The flow is illuminated with a double-pulsed Nd: YAG laser (120 mJ pulse energy) at a wavelength of 532 nm. The laser sheet is generated by a plano-convex spherical lens with a 750 mm focal length along with a plano-concave cylindrical lens with a focal length of -12.77 mm. Hollow glass spheres with a mean diameter of 65 μm and a density of 0.21 gr/cm^3 are used as tracer particles. Double frame images are captured with two 12-bit HiSense MkII CCD cameras with a sensor resolution of 1344 × 1024 px^2, positioned side-by-side to expand the size of the field of view. The right camera is positioned at a relatively low position to properly acquire the flow field around the wing trailing edge. A Nikon 50 mm lens is used for each

camera, and the aperture of the lens ($f\#$) is set to 2. The mapping information obtained from the calibration target image is used to stitch the double-frame camera images.

The size of the resultant stitched images is 2302 × 1338 px^2. The time between two frames (i.e., the time between two laser pulses) is set to 9 ms. The scale factor is 9.3 px/mm for both cameras, yielding a field of view (FOV) of 247.5 × 143.9 mm^2, as shown in Figure 3. In each set of experiments, images are captured at sixteen stages with 0.25 chord length spacing between them. Figure 3 shows the PIV setup configuration and the field of view.

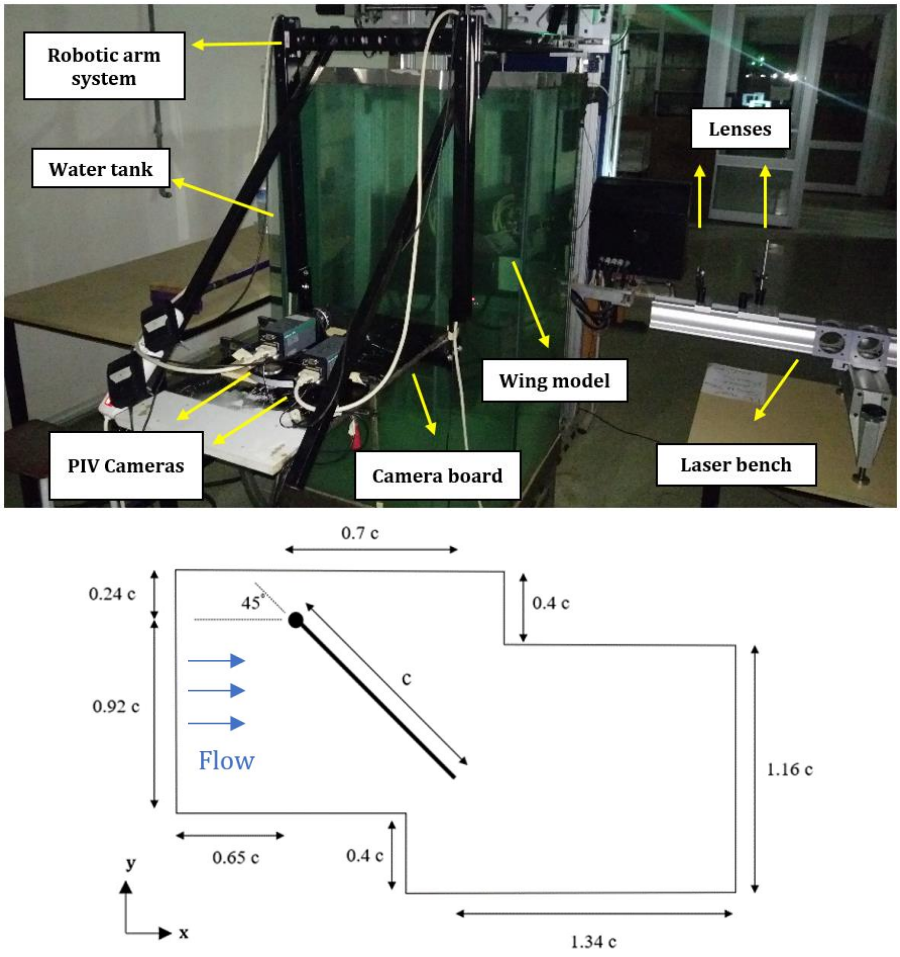

Figure 3. Top: Experimental setup for the PIV measurements. Bottom: Wing position and field of view.

2.4. Data Processing

Image preprocessing, calibration, and vector calculations are performed in Dantec Dynamic Studio 2015a software. Image preprocessing includes masking, background noise removal, and image balancing with a 15×15 smooth cell size balance image, which are performed to

augment the image quality. Subsequently, the stitched images are cross correlated with an interrogation area size of 64 × 64 px^2 with 75% overlap, resulting in 1.72 mm vector spacing and 53 vectors/c vector resolution. The erroneous velocity vectors are detected and substituted by the use of the universal outlier detection technique [14]. The experiments are repeated eight times for each phase, and the resultant velocity vector fields are ensemble-averaged to enhance the signal-to-noise ratio of the velocity measurements. The ensemble-averaged velocity fields are then used for further analysis and presented in this paper.

The circulation of the leading-edge vortex is calculated by use of the out-of-plane vorticity ($\Gamma_{LEV} = \oint \omega_z dxdy$, where ω_z is the out-of-plane component of vorticity) and it is non-dimensionalized by the terminal velocity and chord ($\Gamma^*_{LEV} = \Gamma_{LEV}/c\ V_t$). The LEV centroid coordinates are acquired by the γ_1 method introduced by Graftieaux et al. [15]. The non-Galilean invariant scalar γ_1 function is defined as:

$$\gamma_1(\mathrm{P}) = \frac{1}{N}\sum_{M} \frac{(\mathbf{L}_{PM} \times \mathbf{U}_M) \,.\, \boldsymbol{z}}{\|\mathbf{L}_{PM}\|.\|\mathbf{U}_M\|} = \frac{1}{N}\sum_{M} \sin\theta_M \tag{3}$$

where N is the number of grid points M inside the definable area surrounding P and M, and $\boldsymbol{z}$ is the unit normal vector to the measurement plane. $\mathbf{U}_M$ is the velocity vector, $\mathbf{L}_{PM}$ is the radius vector from the grid points to the velocity vectors, and θ_M is the angle between position vector and the velocity vector. Equation (3) is the cross product of the velocity vector and radius vector over the multiplication of their magnitudes, which results in sin θ_M. The γ_1 has values from 0 to 1, and the vortex core is the point where γ_1 has the highest value $\|\gamma_1\|$.

The vortex boundary can be identified by the calculation of γ_2 function, which is a Galilean invariant scalar function, defined as:

$$\gamma_2(\mathrm{P}) = \frac{1}{N}\sum_{M} \frac{\left(\mathbf{L}_{PM} \times (\mathbf{U}_M - \mathbf{U}_p)\right) \,.\, \boldsymbol{z}}{\|\mathbf{L}_{PM}\|.\left\|\mathbf{U}_M - \mathbf{U}_p\right\|} \tag{4}$$

where $\mathbf{U}_p$ is the local convection velocity. The region that $\gamma_2 > 2/\pi$ is defined as the LEV circulation region in the calculations [15]. The reader is referred to [16], [17], [18] for more detailed information regarding the experimental setup and data processing methods.

3. RESULTS

3.1. Temporal Change of the Geometric Angle of Attack

During the motion, the rigid wing has a fixed angle of attack, whereas it changes for the flexible wings due to structural deformations. The angle between the chord line and the rectilinear motion direction is defined as the geometric angle of attack. The temporal variation of the geometric angle of attack for the wings with a chordwise flexibility at 75% of their span position is depicted in Figure 4. The wing with a high degree of flexibility undergoes a larger chordwise deformation compared to the wing with an intermediate

degree of flexibility. Considering that the resultant force direction is normal to the chord line for revolving flexible wings at a high angle of attack, as claimed by van de Meerendonk et al. [12], the resultant force vector is inclined more toward the lift direction due to the relatively low geometric angle of attack in the case of the high degree of flexibility. For the wing with an intermediate degree of flexibility, the geometric angle of attack shows a significant variation during the acceleration phase (until $\delta^* = 1$), after which it has a more-or-less constant value. For the wing with a high degree of flexibility, the geometric angle of attack declines even after the initial speed-up phase.

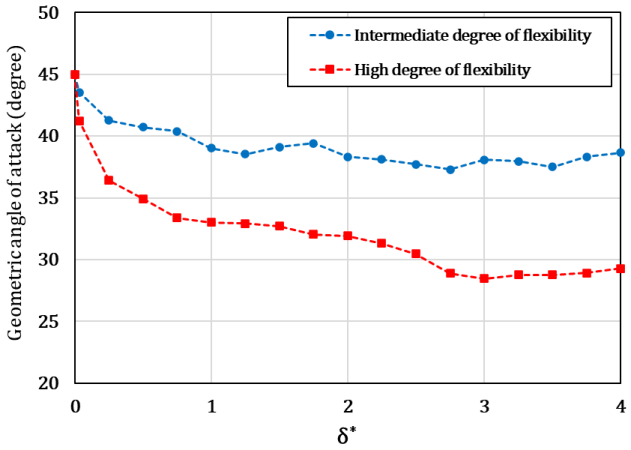

Figure 4. Temporal change of the geometric angle of attack for the wings with chordwise flexibility at the 75% span position.

3.2. Flow Field Characteristics

Contours of the out-of-plane vorticity at the 75% span position for $\delta^* = 0.5, 1, 1.5, 2, 3,$ and 4 are given in Figure 5. In general, a similar flow topology that is comprised of a coherent LEV and a series of trailing-edge vortices (TEVs) is observed in all cases in the acceleration phase. At the end of the acceleration phase, the LEV is slightly lifted-off from the surface of the wing and it has a fragmented structure, which is in accordance with the literature [19]. In the subsequent stages of the translational motion, the LEV continues to move away from the surface of the rigid wing and the wing of intermediate flexibility, and it bursts into smaller clusters of vortical structures. At $\delta^* = 3$, a coherent series of TEVs is observed in the wake, and the shear layers originating from the leading edge and the trailing edge interact. This interaction yields small-scale vorticity structures filling the wake of the rigid and intermediate flexibility wings. For these wings, after $\delta^* = 3$, the flow is mostly detached from the wing surface, which gives way to a chaotic flow field with stretched incoherent positive vorticity layers originating from the leading edge. On the other hand, the flow stays attached to the high flexibility wing surface due to sizeable chordwise deformation and the associated relatively low angle of attack of the wing. In this case, the LEV

stays closer to the wing surface. The flow preserves its coherency event at later phases of the motion, which can be linked to the reattachment of the flow after the flow separation at the leading edge so that it leaves the trailing edge tangentially (see Figure 6). Contours of velocity magnitude complemented with streamlines at $\delta^* = 1, 2, 3, \text{and } 4$ for all of the wings are shown in Figure 6. Flow separation at the leading edge occurs in all cases, which is followed by a reattachment to the wing surface at $\delta^* = 1$. The lift-off of the LEV and completely separated flow at later stages of the motion are clearly visualized for the rigid and the intermediate degree of flexibility cases by means of the streamlines. The flow reattachment downstream of the LEV persists even at later phases in the high degree of flexibility case, which results in the flow leaving the trailing edge smoothly. In this case, the LEV moves with the wing and stays closer to the wing surface.

3.3. LEV Characteristics

Figure 7 depicts the temporal variation of the normalized LEV circulation (Γ^*_{LEV}) for all cases. The rigid wing generates a greater LEV both in size and in circulation for the most part of the motion. The maximum LEV circulation value is reached at $\delta^* = 1.75$ in the rigid wing case, after which the LEV bursts into smaller-scale flow structures and the circulation level decreases abruptly. The circulation of the LEV for the wing with a high degree of flexibility is relatively low, indicating the formation of a relatively weak low-pressure region due to the LEV on the upper surface of the wing and thus the generation of relatively small forces. This may seem to be a drawback in terms of lift generation, but the size of the horizontal surface area and the distance of the vortex core to the wing surface should be considered in the assessment of vortex-related force. The wing of high flexibility is advantageous in terms of the size of the horizontal area due to the elevated chordwise deformation of the wing (see Figure 4). The evaluation of the latter is done in Figure 8.

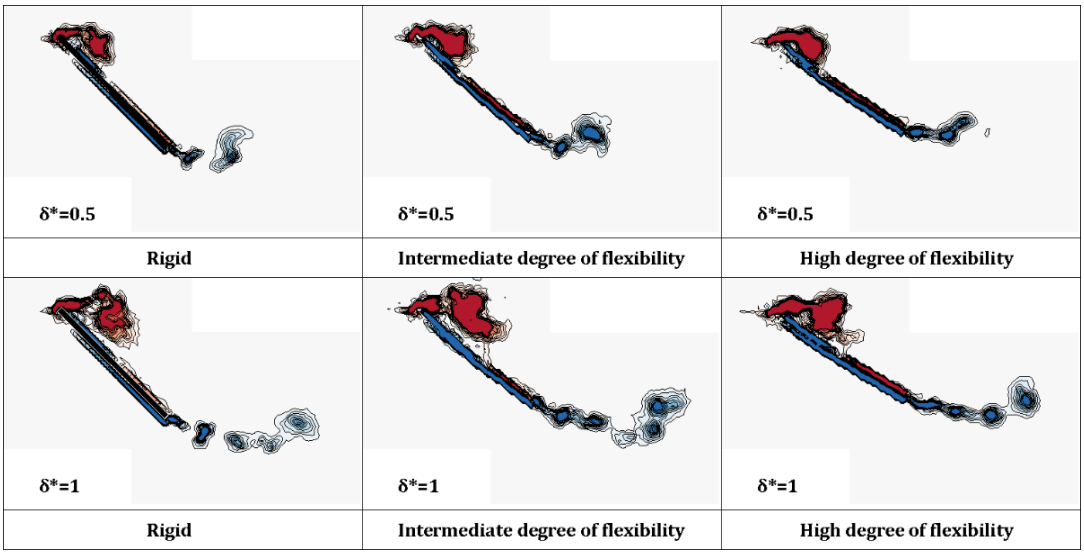

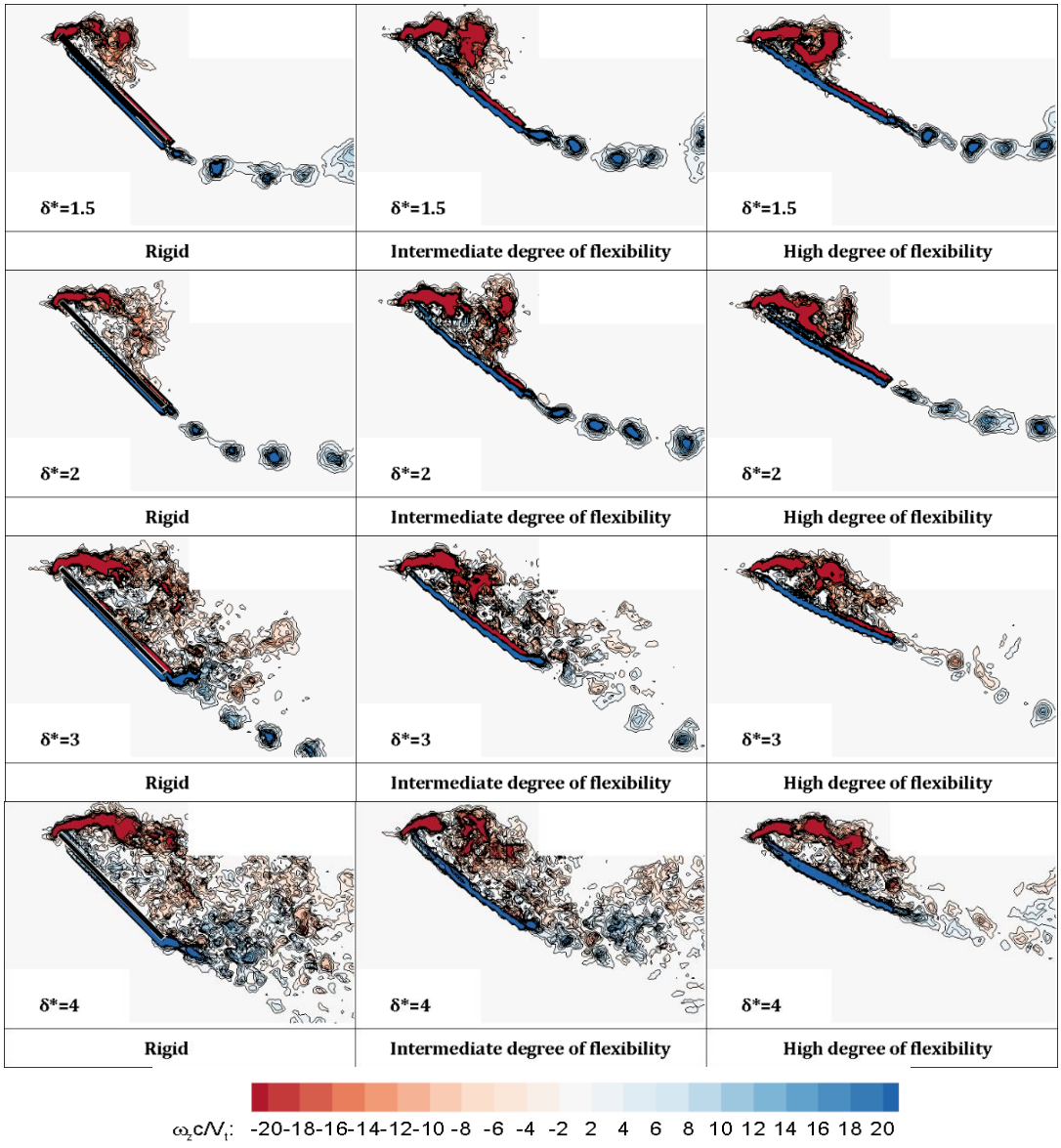

Figure 5. The z-component of vorticity contours ($\omega_z c/V_t$) at the 75% span position at six stages of motion.

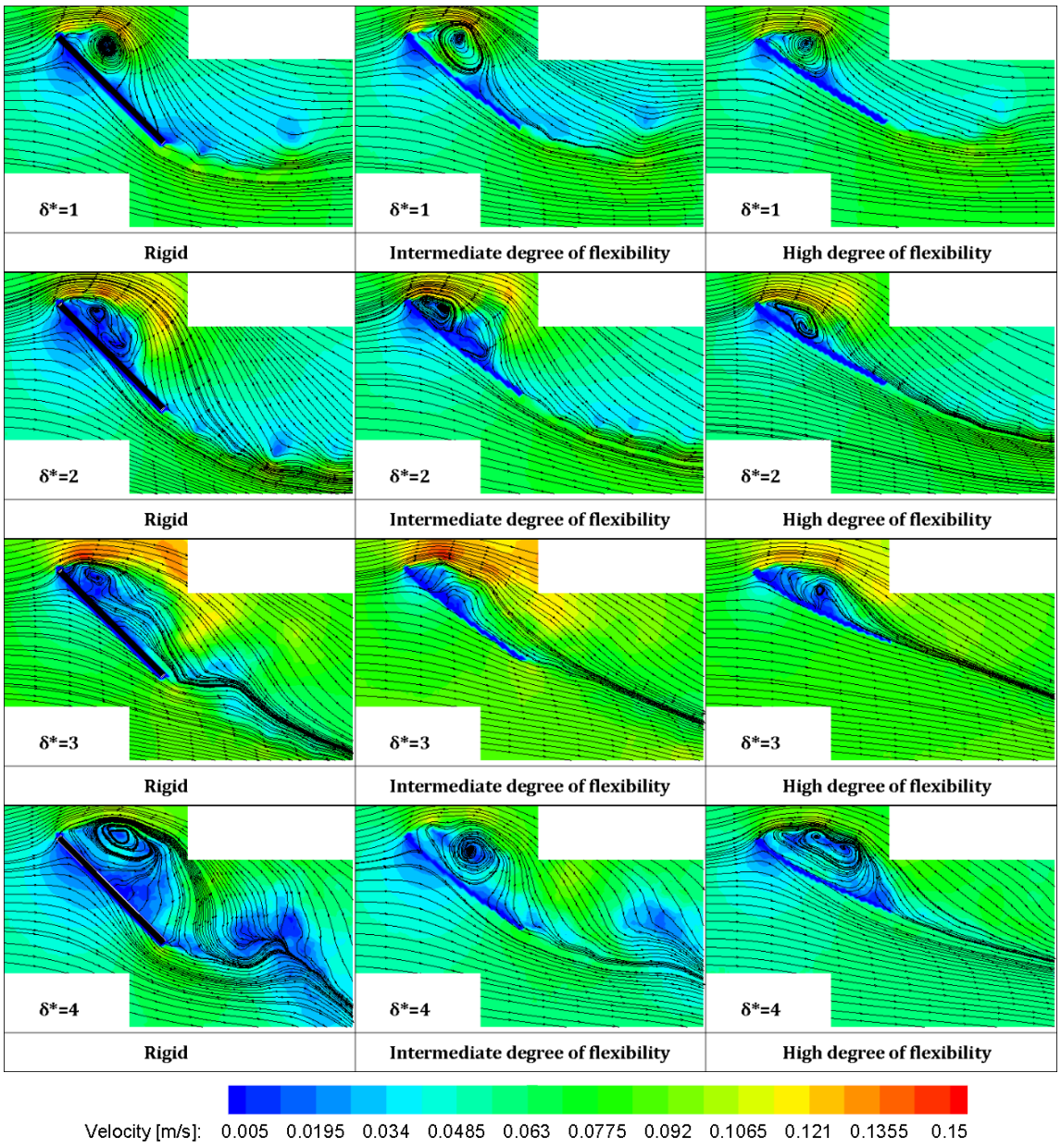

Figure 6. Contours of velocity magnitude along with streamlines at four stages of motion.

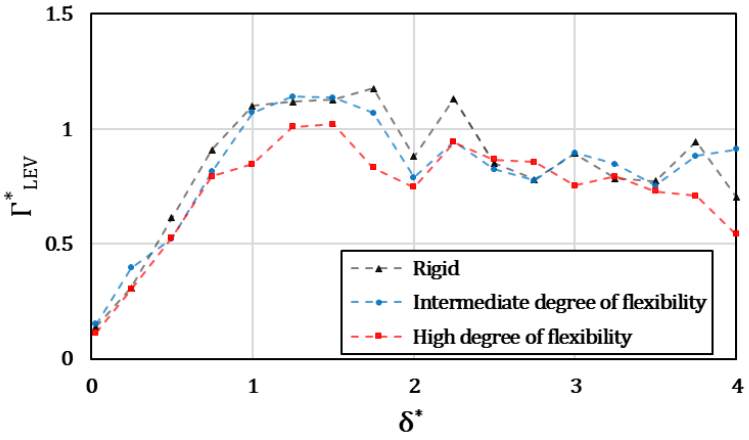

Figure 7. Temporal evolution of LEV circulation.

The position of the first LEV is tracked throughout the motion by the use of the γ_1 integral method. The diagonal distance between the leading edge and the leading-edge vortex core (S_1), and the normal distance between the core of the LEV and the surface of the wing (S_2) are calculated and presented in Figure 8. In the acceleration phase, the LEV centroid has approximately the same trajectory in all cases. For the rigid and intermediate degree of flexibility wings, a single vortex centroid cannot be detected after 1.75 chords of travel due to the shedding and bursting of the LEV into smaller structures. On the other hand, in the high degree of flexibility case, the LEV stays closer to the wing surface, keeps its coherency for a longer time, and moves with the wing. According to the vorticity-moment theorem described by Wu [20], the circulatory component of the force acting on a body can be obtained from the time rate of change of the total first moment of the vorticity field (calculated with respect to an inertial reference frame) in the complete fluid domain. In this respect, an LEV that is moving with the wing contributes to the force generation continuously due to the increase of the moment arm in the calculation of the moment of vorticity. Therefore, a stable LEV that is moving with the wing for an extended period of motion may boost force generation despite its relatively small strength. In addition, its presence close to the wing surface may be considered another factor that contributes to force generation.

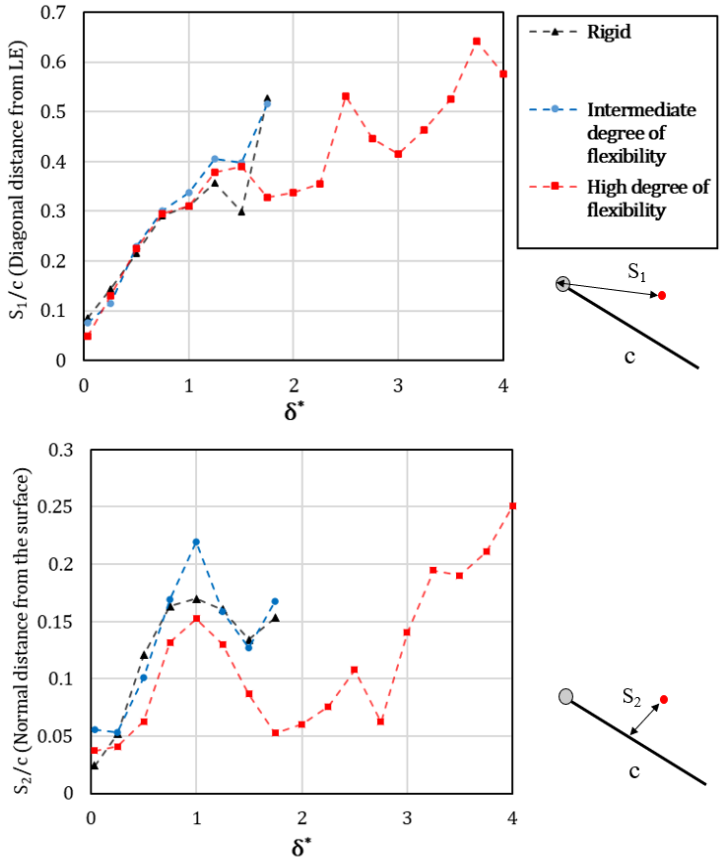

Figure 8. Top: Temporal change of the LEV centroid diagonal distance from the leading edge. Bottom: Temporal change of the normal distance between the LEV centroid and the wing surface.

4. CONCLUSION

This study explores the flow fields around surging-translating flat plates with three different chordwise flexural stiffness values. The phase-locked two-dimensional, two-component particle image velocimetry technique is used in order to obtain velocity fields in a plane that is aligned with the 75% span position of the wings. Three different wings are tested in this study: a rigid wing made of acrylic glass with a thickness of 1000 μm; two flexible wings made of polyethylene terephthalate with a thickness of 175 μm and 125 μm to investigate the effect of wing deformation on the characteristics of the LEV. The translating-surging motion kinematics consists of an acceleration phase during which the wings start their motion from rest and accelerate to a terminal speed over a chord length of travel at a fixed angle of attack of 45° and a constant-speed phase that lasts for three-chord lengths of travel. The Reynolds number based on the terminal velocity and the wing chord length is 7360.

The comparison of the geometric angles of attack reveals that the wing with a high degree of flexibility undergoes a large amount of wing deformation, yielding a decrease in the geometric angle of attack from the initial value of 45° to approximately 29° at the last stages of the constant speed phase. This decrease occurs both in the acceleration phase and the constant-speed phase. On the other hand, for the wing with an intermediate degree of flexibility, the geometric angle of attack varies only during the acceleration phase and stays constant at around 38° in the constant-speed phase.

A coherent LEV and a number of TEVs are present in all cases in the acceleration phase of the motion. In the constant-speed phase, on the other hand, the flow fields display significant variations. In the high degree of flexibility case, the flow reattaches on the wing surface downstream of the flow separation at the leading edge. Accordingly, a coherent LEV moves with the wing throughout the motion. In the rigid and intermediate degree of flexibility cases, the LEV lifts off from the wing surface and bursts into small-scale structures in the late stages of the constant-speed phase. Greater LEV circulation levels are achieved in the rigid and intermediate degree of flexibility cases compared to the wing of high flexibility. This can be attributed to the larger wing deformation and smaller geometric angle of attack of the wing with a high degree of flexibility. On the other hand, the LEV preserves its coherency, stays close to the wing surface, and moves with the wing of high flexibility throughout the translational motion. The presence of a stable LEV close to the wing surface and the larger size of the horizontal area that the LEV-related low-pressure region is acting on in the high degree of flexibility wing case have a positive influence in terms of lift generation even though a relatively weak LEV forms due to the smaller geometric angle of attack.

ACKNOWLEDGMENTS

The authors appreciate the support of Assoc. Prof. Dr. Bas Van Oudheusden from Delft University of Technology.

REFERENCES

[1] D. J. Pines and F. Bohorquez, *Challenges facing future micro-air-vehicle development*, Journal of Aircraft **43**(2), 290-305 (2006).

[2] S. P. Sane, *The aerodynamics of insect flight*, Journal of Experimental Biology **206**(23), 4191-4208 (2003).

[3] F. T. Muijres, L. C. Johansson, R. Barfield, M. Wolf, G. R. Spedding, and A. Hedenstrom, *Leading-edge vortex improves lift in slow-flying bats*, Science **319**(5867), 1250-1253 (2008).

[4] D. Lentik and M. H. Dickinson, *Rotational accelerations stabilize leading edge vortices on revolving fly wings*, Journal of Experimental Biology **212**(16), 2705-2719 (2009).

[5] C. P. Ellington, C. Van Den Berg, A. P. Willmott, and A. L. R. Thomas, *Leading-edge vortices in insect flight*, Nature **384**(6610), 626-630 (1996).

[6] M. V. Ol and H. Babinsky, "Unsteady flat plates: a cursory review of AVT-202 research", in Proc. of the 54th AIAA Aerospace Sciences Meeting, AIAA SciTech 2016, 4-8 January 2016, San Diego, CA, USA [Online]. Available: https://arc.aiaa.org. [Accessed: 2 Jan. 2016].

[7] W. Shyy, H. Aono, S. K. Chimakurthi, P. Trizila, C. K. Kang, C. E. Cesnik, and H. Liu, *Recent progress in flapping wing aerodynamics and aeroelasticity*, Progress in Aerospace Sciences **46**(7), 284-327 (2010).

[8] L. Zhao, Q. Huang, X Deng, and S. P. Sane, *Aerodynamic effects of flexibility in flapping wings*, Journal of the Royal Society Interface **7**(44), 485-497 (2010).

[9] N. Beals and A. R. Jones, Lift production by a passively flexible rotating wing, AIAA Journal **53**(10), 2995-3005 (2015).

[10] A. M. Mouncastle and T. L. Daniel *Animal Locomotion*. Berlin, Germany: Springer, 2010, pp. 311-320.

[11] J. D. Eldredge, J. Toomey, and A. Medina, *On the roles of chord-wise flexibility in a flapping wing with hovering kinematics*, Journal of Fluid Mechanics **659**, 94-115 (2010).

[12] R. van de Meerendonk, M. Percin, and B. W. van Oudheusden, *Three-dimensional flow and load characteristics of flexible revolving wings*, Experiments in Fluids **59**(10), 1-22 (2018).

[13] M. Percin, Y. Hu, B. W. van Oudheusden, B. Remes, and F. Scarano, *Wing flexibility effects in clap-and-fling*, International Journal of Micro Air Vehicles **3**(4), 217-227 (2011).

[14] J. Westerweel, and F. Scarano, *Universal outlier detection for PIV data*, Experiments in Fluids **39**(6), 1096-1100 (2005).

[15] L. Graftieaux, M. Michard, and N. Grosjean, *Combining PIV, POD and vortex identification algorithms for the study of unsteady turbulent swirling flows*, Measurement Science and Technology **12**(9), 1422-1429 (2001).

[16] M. Yazdanpanah, "Flow Characteristics of Translating Flexible Wings at Low Reynolds Numbers," M.Sc. thesis, Aeronautical Engineering, Middle East Technical University, Ankara, Turkey, 2019.

[17] M. Yazdanpanah, H. Amiri, M. Percin, R. van de Meerendonk, and B. W. van Oudheusden, "Flow field characteristics of translating and revolving flexible wings," in *10th Ankara International Aerospace Conference, AIAC 2019, 18-20 September 2019, Ankara, Turkey* [Online]. Available: http://aiac.ae.metu.edu.tr. [Accessed: 20 Sep. 2019].

[18] M. Percin, M. Yazdanpanah, H. Amiri, R. van de Meerendonk, B. W. van Oudheusden, "Flow Field Characteristics of Translating and Revolving Flexible Wings," in *Proc. of the 13th International Symposium on Particle Image Velocimetry, ISPIV 2019, 22-24 July 2019, Munich, Germany* [Online]. Available: https://pure.tudelft.nl. [Accessed: 24 July. 2019].

[19] M. Percin and B. W. van Oudheusden, *Three-dimensional flow structures and unsteady forces on pitching and surging revolving flat plates*, Experiments in Fluids **56**(2), 1-19 (2015).
[20] J. C. Wu, *Theory for aerodynamic force and moment in viscous flows*, AIAA Journal **19**(4), 432-441 (1981).

To Cite This Article: M.Yazdanpanah, M.Perçin, *Leading-Edge Vortex Characteristics of Surging-Translating Flexible Wings*, Journal of Aeronautics and Space Technologies **16**(1), 64-79 (2023).

VITAE

Mahdi Yazdanpanah is currently a Ph.D. student in Aerospace Engineering at the Aerospace Engineering Department of Middle East Technical University (METU), Ankara, Turkey. He received his B.Sc. degree in Aerospace Engineering from Science and Research branch of Azad University, Tehran, Iran, in 2016. He received his M.Sc. degree in Aerospace Engineering from Middle East Technical University, Ankara, Turkey, in 2019.

Mustafa Perçin is currently an Assistant Professor at the Aerospace Engineering Department of Middle East Technical University (METU), Ankara, Turkey. He received his B.Sc. degree in Aeronautical Engineering from Istanbul Technical University, Istanbul, Turkey, in 2007. He received his M.Sc. degree in Aeronautical-Astronautical Engineering from Istanbul Technical University, Istanbul, Turkey, in 2009. He took his Research Master's degree at the Environmental and Applied Fluid Dynamics department of the von Karman Institute for Fluid Dynamics, Rhode-Saint-Genése, Belgium, in 2010. He received his Ph.D. from Delft University of Technology, Delft, the Netherlands, in 2015.